Investigating the wind-wave interaction on mean wind and turbulence structure using COAWST with WRF-LES during a storm event

Sima Hamzeloo[a], Xiaoli Guo Larsén[a], Alfredo Peña[a], Jana Fischereit[a], and Oscar García-Santiago[a]

[a]Technical University of Denmark, Frederiksborgvej 399, Roskilde 4000, Denmark

Correspondence: Sima Hamzeloo (siham@dtu.dk)

Abstract. We investigate wind-wave interactions within the marine atmospheric boundary layer during a storm event over the North Sea using a multiscale coupled modeling framework. Large eddy simulation (LES) domains within the Weather Research and Forecasting model have been coupled with the Simulating WAves Nearshore (SWAN) model through the Coupled Ocean-Atmosphere-Wave–Sediment Transport (COAWST) system. The simulation consists of six nested domains, three outer mesoscale domains with horizontal grid spacings of 9.9, 3.3, and 1.1 km, and three inner large eddy simulation domains with coarse (100 m) and fine horizontal grid spacings. Wind and wave outputs from both the finest mesoscale domain and the coarsest LES domain are evaluated against metocean and lidar measurements collected during the storm. The results show that the coarsest LES domain represents wind speeds up to 150 m height more accurately than the mesoscale output, but due to excessive simulated vertical wind shear. Above this height, the mesoscale and LES winds become much closer, both overestimating the measured winds. The measured wind direction is well captured across both types of domains. The significant wave height, peak wave period, and mean wave direction simulated by SWAN show better agreement with observations when forced by the LES output than the mesoscale output. Additionally, the coupled simulations exhibit stronger turbulence fluxes than the uncoupled simulations, which is clearly observed in the vertical profiles of velocity variances and covariances. These findings demonstrate the impact of high-resolution coupled modeling for capturing offshore boundary layer dynamics and on wind and wave predictions under severe weather conditions.

1 Introduction

Accurate understanding of the structure of the marine atmospheric boundary layer (MABL), including mean wind profiles and turbulence characteristics, has become increasingly important in recent decades due to the global expansion of offshore wind energy, and it is listed as one of the grand challenges for wind energy research (Shaw et al., 2022). The physical processes in the MABL can be more complex than those over land due to additional interactions at the air-sea interface, which span multiple temporal and spatial scales. These interactions, particularly involving ocean waves, can modify the atmospheric flow up to hub height and above (Kalvig et al., 2014; Yang et al., 2014; Fischereit et al., 2022), affecting wind resource assessments, turbine loading, and energy yield predictions. Such complexities require advanced, high-resolution modeling strategies (Shaw et al., 2022).

Atmospheric motions within the MABL are impacted by mesoscale weather systems down to turbulent eddies. Numerical models are typically designed to operate at a range of scales, and as a result, studies often rely on a variety of parameterizations and configurations to bridge the gap between mesoscale and microscale dynamics, (Chow et al., 2019). Our understanding of coupled wind–wave dynamics has been limited by the difficulty of capturing at the same time both mesoscale weather variability and microscale turbulence over realistic ocean surfaces. To address this, Ning et al. (2023) evaluated parameterizations of sea surface roughness in a multiscale simulation framework, employing the Weather Research and Forecasting (WRF) model coupled with the Simulating of WAve Nearshore (SWAN) model for mesoscale processes. The output of the wave-influenced roughness parameterization was fed into the Parallelized Large-eddy Simulation Model (PALM) rather than being directly coupled to the wave model. Their results showed that, although the framework reproduced mean wind and turbulence characteristics under realistic offshore conditions, it exhibited minimal sensitivity to the different roughness parameterizations. Additionally, their use of a one-way, meso-to-micro coupling meant that full two-way interactions between scales were not accounted for. They suggested that future work should explore two-way coupling strategies and more advanced wind–wave parameterizations.

These limitations underscore the need for a multiscale modeling framework that integrates mesoscale and microscale processes. Such approaches allow for nesting LES domains within mesoscale simulations, enabling the representation of both synoptic-scale variability and turbulence. In these frameworks, mesoscale atmospheric conditions provide realistic time-varying boundary forcing for the embedded LES, allowing us to partly resolve turbulence with the possibility of wave-induced feedback that would otherwise be missed in coarser simulations. Multiscale simulations driven by time-varying atmospheric conditions were shown to be able to represent meteorological processes on land with large-scale variations in wind and temperature, as well as the associated turbulent flow structures across scales (Muñoz-Esparza et al., 2017). In the present work, the meso-to-micro coupling is extended to offshore conditions, where both the mesoscale and the LES domains are explicitly coupled with a wave model to represent wind–wave interactions in the MABL, which has not been fully addressed in earlier multiscale studies.

The Coupled Ocean-Atmosphere-Wave-Sediment Transport (COAWST) modeling system (Warner et al., 2010) is a well-established tool for simulating air-sea interactions. The COAWST framework integrates several modeling components comprising the model coupling toolkit to exchange data fields between an ocean model (ROMS), an atmospheric model (WRF), a wave model (SWAN), and a sediment transport model. Numerous studies have utilized COAWST to investigate a variety of air–sea interaction processes (Cambazoglu et al., 2024; Jiang et al., 2025). To our knowledge, to date, all coupling between the components of the WRF and SWAN models within the COAWST framework has been performed at mesoscale resolutions. For example, in the field of offshore wind energy, studies have examined interactions between wind, waves, and wakes (Larsén et al., 2024; Fischereit et al., 2022), while others have focused on hurricanes and extreme tropical cyclones (Chen et al., 2024; Alimohammadi et al., 2020; Olabarrieta et al., 2012). Larsén et al. (2019) used COAWST to compare roughness-length parameterizations with direct stress coupling for wave–atmosphere interactions. They found that stress-based coupling better captured the wind field measured by synthetic aperture radar over a coastal, shallow water area.

Here, we focus on an extreme wind and wave event, following our previous study (Hamzeloo et al., 2025), in which we investigated the effects of waves on mean wind speed, direction, turbulence fluxes and spectral characteristics using a one-way offline coupling between WRF-LES and the MIKE3 Wave FM model (M3W) (DHI, 2024). The latter study was conducted under idealized conditions. Here, we build on that work by performing a fully coupled weather-driven multiscale simulation using WRF and SWAN, allowing for a more realistic assessment of wave effects on MABL dynamics.

This paper is structured as follows: Section 2 describes the methodology, including a description of the measurement data, the model setup for both wind and wave components, and the coupling strategy. Section 3 presents the simulation results. Sections 4 and 5 provide discussion and conclusions, respectively.

2 Methodology

2.1 Measurements and the selected case

We use wind and wave measurements from the Reducing the Uncertainty of Nearshore Experiment (RUNE) project to evaluate wind and wave simulations. RUNE was a collaborative research project that conducted a coastal offshore measurement campaign from November 2, 2015, to March 1, 2016, near the west coast of Jutland, Denmark. The experiment and data collected during RUNE are described in detail by Floors et al. (2016) and Bolaños and Rørbæk (2016).

During the campaign, wind and wave measurements were taken approximately 7 km offshore. Wave measurements were obtained using a directional Triaxy wave buoy equipped with a downward-looking acoustic Doppler current profiler. This buoy was deployed at the beginning of the campaign at a water depth of 16.5 m. The hourly integrated wave parameters—including significant wave height (H_s), maximum wave height (H_{max}), peak wave period (T_p), average zero-crossing period (T_{02}), and mean wave direction (MWD) are processed from the 7 Hz sampled data. A lidar buoy, positioned less than 200 m from the wave buoy, was equipped with a WindCube® v2 Doppler wind lidar to record wind data. Mean wind speed and direction are available every 10 min at 12 different heights above mean sea level: 40, 47, 59, 79, 97, 117, 134, 147, 172, 197, 209, and 247 m. Figure 1 shows the geographical location of the RUNE measurements as a red dot.

Figure 2 presents the time series of H_s and the wind speed at a height of 40 m, MWD, and the wind direction at a height of 40 m, for a period of a week around our focus day. The wind measurements shown in the plots correspond to the lowest recorded height. We observe a wind-wave alignment from the southwest (less than 60 degree difference), which lasts for almost a full day on the 5th of December, marked as gray in Fig. 2. Additionally, the most intense wave event during the measurement period occurred on the same day at 18:00 UTC, with $\mathrm{H}_s = 5.77$ m and $T_{02} = 8.7$ s. During this storm, the average wind speed ranged from 21.3 m s^{-1} at 40 m to 26.8 m s^{-1} at 247 m. We use this day to investigate the wind-wave interaction in the COAWST modeling system in LES mode.

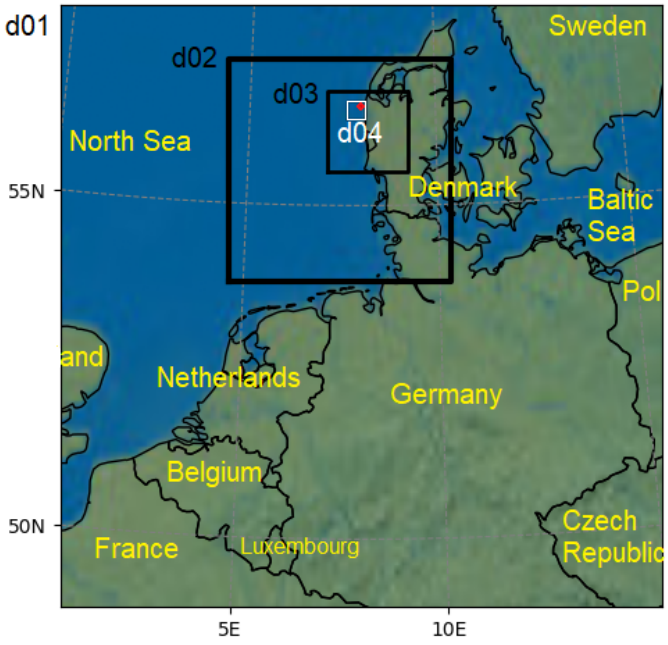


Figure 1. Nested domains' configuration of our simulations. The red dot in the upper right of domain D04 is the location of RUNE measurements. Domains D05 and D06 located within D04 are not shown.

2.2 Modeling system

We utilize the WRF model, version 4.5 (Skamarock et al., 2019) and SWAN model, version 41.45 (Booij et al., 1997) through the COAWST modeling system version 3.8 (Warner et al., 2010) to simulate wind-wave interactions in the North Sea for the selected storm. Other components of the COAWST system are not activated in this study. The WRF and SWAN models are two-way, online, coupled through the wave boundary layer model (WBLM) implemented in SWAN (Du, 2017; Du et al., 2019). The WBLM accounts for the vertical variation of stresses and energy in the wave boundary layer (WBL), which is the interface between the waves and the atmospheric boundary layer above it. In this region, the wind speed profile deviates from the classical logarithmic shape due to wave-induced motions and momentum exchange. In this coupled system, the WRF horizontal velocity components at the height of 10 m (longitudinal U and meridional V) are sent to SWAN. The WBLM uses the former velocities along with local wave-induced and turbulent stress, and wave phase velocity, to calculate the vertical wind profile within the WBL by solving the kinetic energy conservation equation, computes the equivalent roughness length (z_0) that conforms to the logarithmic wind profile, and finally transfers z_0 back to the surface-layer module of the WRF model (Fischereit et al., 2022; Du et al., 2022). This results in more realistic wave growth and improved energy exchange at the air–sea interface.

Unlike most previous COAWST applications, which remain limited to mesoscale resolutions, our configuration extends the coupling to include LES domains. To make this framework operational, we applied two key adjustments. First, in the finer

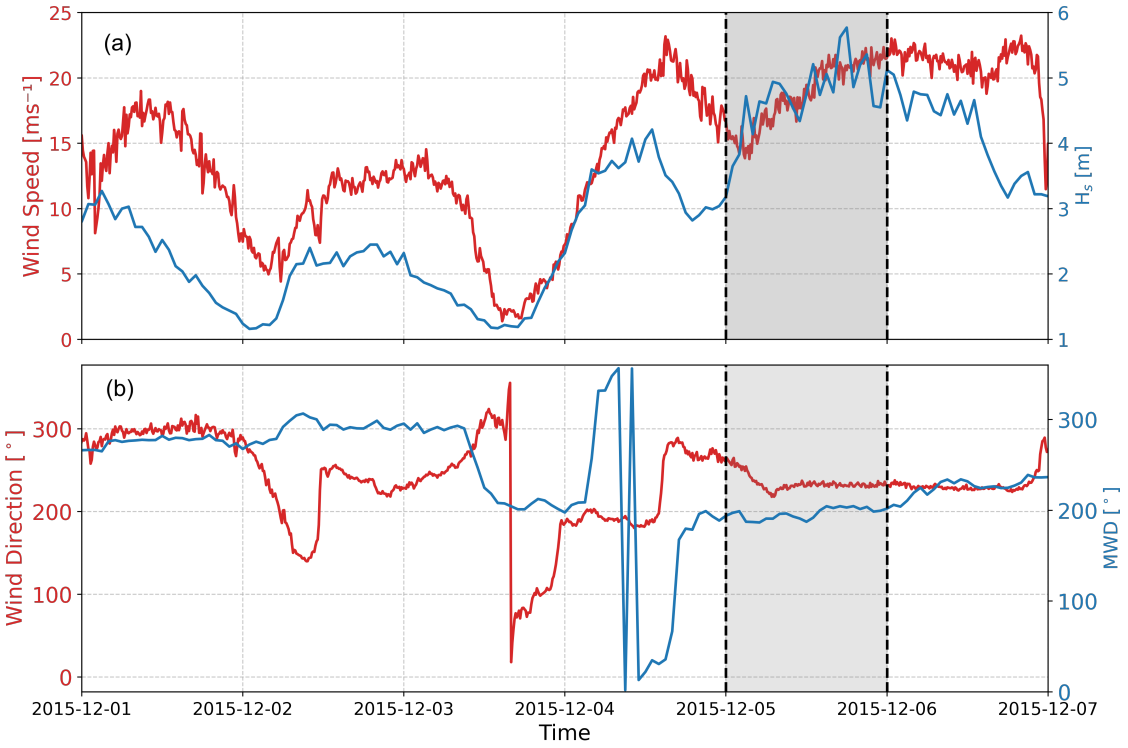


Figure 2. Time-series of wind speed (a) and direction (b) on the left axis and significant wave height H_s (a) and mean wave direction (MWD) (b) on the right axis, from measurements of the wave buoy and the lidar at a 40-m height, respectively. The gray range shows the period we selected for this study.

domains with 100 m horizontal grid spacing, we replaced the planetary boundary layer (PBL) scheme with LES. Second, we implemented the cell perturbation method (CPM) (Muñoz-Esparza et al., 2015; Muñoz-Esparza and Kosović, 2018) in the WRF model within the COAWST framework to enable turbulence simulations.

2.3 Simulations

Our multiscale WRF simulations include six nested domains. The outer three domains run in mesoscale mode with horizontal grid spacings of 9.9, 3.3, and 1.1 km, respectively, while the inner three domains run in LES mode. The coarsest LES domain has a grid spacing of 100 m. The grid spacing ratio between mesoscale domains is 1:3, while the ratio from the finest mesoscale to the coarsest LES domain is 1:11. In addition, we nest two more LES domains with a 1:5 grid spacing ratio of 20 m and 4 m, which are run for a shorter period (10 hr). The time step ratio matches the grid spacing ratio, with a time step of 45 s for the outermost mesoscale domain. All four domains consist of 61 vertical levels, with the first level located at 10 m above the surface. The model's top is at 5000 Pa. The SWAN model adopts the same domain configuration as presented in Fig. 1. More details on the model domain specifications can be found in Table 1.

The coarsest 100-m grid spacing LES domain (D04) is intentionally selected as it reflects what is commonly used in industry and operational multiscale modeling (Vortex FdC, 2018; Kshetri and Momen, 2025), where computational constraints limit the LES domain sizes. Although the LES domains use a 1.5-order TKE-based SGS model, the coarse horizontal grid spacing does not allow a large portion of the turbulence field to be explicitly resolved for this particular storm event, and therefore, a substantial fraction of the turbulent stresses is originated from the SGS model. The finer-resolution LES domains (D05 and D06) are included to partly illustrate how higher resolution increases the fraction of resolved turbulence.

Table 1. Domain configurations of the simulations. Δx corresponds to horizontal grid spacing, N_x and N_y to number of grid points in the x (west-east) and y (north-south) direction and Δt to numerical integration time step.

Simulations	Domains	Δx [m]	Nest Ratio	$N_x \times N_y$	Δ t [s]	PBL/SGS
WRF/	D01	9900	–	101×101	45	YSU
WRF-SWAN	D02	3300	3	112×112	15	YSU
	D03	1100	3	121×121	5	YSU
WRF-LES/	D04	100	11	309×276	0.450	Deardorff
WRF-LES-SWAN	D05	20	5	301×301	0.090	Deardorff
	D06	4	5	301×301	0.018	Deardorff

The outermost domain is initialized and forced using ERA5 reanalysis data, updated every six hours (C3S, 2017). In addition, the Operational Sea Surface Temperature and Sea Ice Analysis (OSTIA) dataset (Donlon et al., 2012) is used to update the sea surface temperature and sea ice fields during simulations every six hours. For static inputs, we utilize the default datasets provided by the WRF model, along with the CORINE land cover dataset (Feranec, 2016) and the ESA Climate Change Initiative (CCI) land cover datasets at resolutions of 100 m and 300 m, respectively (Bontemps et al., 2013).

For the physics parameterizations of the WRF model, we employ the WRF Single-Moment 6-Class (WSM 6-class) graupel scheme for microphysics (Hong et al., 2004), which includes predictive variables for water vapor, cloud water/ice, rain, snow, and graupel. For radiation processes, we utilize the Rapid Radiative Transfer Model (RRTM) (Mlawer et al., 1997) for longwave radiation and the Dudhia scheme (Dudhia, 1989) for shortwave radiation, both executed every 9 min. The Kain-Fritsch scheme (Kain and Fritsch, 1993) is employed for cumulus parameterization, activated every 5 min exclusively for the outermost domain. The Unified Noah land surface model (Tewari et al., 2004) is applied for land surface, while the Revised MM5 Monin-Obukhov scheme is used for the surface layer. The Yonsei University (YSU) scheme (Hong et al., 2006) is used for PBL parameterization, which was selected based on a sensitivity analysis among three other schemes: the Mellor-Yamada-Nakanishi-Niino (MYNN) (Nakanishi and Niino, 2006), Mellor-Yamada-Janjic (MYJ) (Janjic, 2002), and Quasi-Normal Scale Elimination (QNSE) (Sukoriansky et al., 2005) schemes. PBL schemes are deactivated for the innermost domains as they run in LES mode with a subgrid-scale (SGS) model that uses a 1.5-order turbulence kinetic energy (TKE) closure (Deardorff, 1980). The closure prognoses the TKE, which is used to compute the local eddy diffusivity.

In multiscale simulations using the WRF model, turbulence in the LES domain may not develop fast enough because of the smooth flow from the parent mesoscale domain and the time needed for high resolution LES domains to develop turbulence.

The PBL scheme assumes horizontal homogeneity within each grid cell, which contrasts with the LES domain, where turbulence is explicitly resolved and an SGS model represents a portion the Reynolds stress tensor and turbulent kinetic energy (TKE) (Muñoz-Esparza et al., 2014). This challenge is further intensified in offshore areas, where the absence of topographical features limits the production of turbulence. To address this issue and promote a seamless transition from mesoscale boundary conditions to fully developed LES turbulence, the CPM is applied at the inflow boundaries of the LES domain. In this study, we integrate the CPM into the WRF model within the COAWST framework for the first time, enabling the application of this technique in coupled ocean–atmosphere–wave simulations. The CPM method (Muñoz-Esparza et al., 2015) introduces controlled perturbations on the potential temperature field. We apply the perturbations on the three contiguous cells of the lateral boundaries to develop realistic turbulent fields (Peña and Mirocha, 2024). Additionally, we conduct a simulation without activating CPM in the LES domain (D04) to assess its impact on the simulations, which is presented in Section 3.5.

We initialize the SWAN model using the output spectrum at each grid cell from a previous simulation conducted 24 hr earlier to allow for spin-up and provide consistent boundary and initial conditions. The open boundaries of the outermost domain are set to zero. This does not impact the innermost domains due to the large domain size. We utilized 36 directional bins with a frequency exponent of 1.1. The frequency range extends from 0.03 to 10.05 Hz, resulting in a total of 61 frequency bins. The SWAN model operates with a time step of 6 min for the four outermost domains, and the time step is reduced to 4 min for D05 and D06. The EMODnet Digital Terrain Model (DTM) with a grid resolution of 1/8 arc-min (approximately 230 m) is used for the bathymetry. In addition to the configurations mentioned above, the SWAN model incorporates several physical processes to accurately simulate wave dynamics. The depth-induced wave break is modeled using the parameters α = 1.0 and γ = 0.73, which control the intensity and the break threshold, respectively. Bottom friction is taken into account using the JONSWAP formulation with a friction coefficient of 0.038, representing energy dissipation due to seabed interactions. White-capping dissipation, which addresses the energy loss from wave breaking in deep water, is activated using the WAM Cycle 3 formulation with drag law fitting. In addition, SWAN considers processes related to sea spray, specifically by modeling whitecapping and wave-induced breaking, which are the primary sources of sea spray. Sea spray is not explicitly modeled as droplets.

Simulations for D01 to D04 are run over a 30-hr period from 18:00 UTC on December 4 to 00:00 UTC on December 6 for both coupled and uncoupled models. Simulations for D05 and D06 are run for a shorter period of 10 h with the same starting time (for both coupled and uncoupled simulations). Results and analysis focus on the entire December 5 for D01 to D04, and on the first 4 hours of this day for D05 and D06, which we use for turbulence analysis. The SWAN model outputs are saved every 10 min for both D03 and D04 domains. For the WRF model, outputs were saved every 10 min for D03 and every 10 s for D04, D05, and D06. All domains share the same spin-up period, despite the shorter total simulation time of D05 and D06.

3 Results

In this section, we first present the surface roughness length (z_0) fields from the finest mesoscale domain (D03) and the coarsest LES domain (D04) for both the coupled and uncoupled simulations. This allows us to quantify the effect of the WBLM on

the surface properties before analyzing its effect on the atmosphere. We then evaluate the outputs from the WRF and SWAN models by comparing simulated wind and wave data from D03 and D04 with RUNE observations at the grid point closest to the measurement site. After the validation, we analyze the turbulence fluxes from D04, D05, and D06. The results from D05 and D06 are not used for validation, as these domains run only for a shorter period, and their purpose is to illustrate the effect of horizontal grid spacing on the resolved and SGS contributions to turbulence.

3.1 Surface roughness

Figure 3 shows distributions of the computed roughness length on 5 December for D03 and D04 from the coupled and uncoupled simulations. The distributions are computed from an area of 6×6 grid points in D03 and the corresponding 66× 66 grid points in D04 around the RUNE location. The figure illustrates the effect of coupling and horizontal resolution on the variability and distribution of roughness length. WRF-LES and WRF-LES-SWAN distributions span over a similar overall range of roughness values, but their shapes differ: WRF-LES appears narrow and Gaussian, while WRF-LES-SWAN is broader and appears Weibull-like. WRF-SWAN also shows more variability compared to WRF; compared to uncoupled versions, both SWAN-versions show lower roughness values.

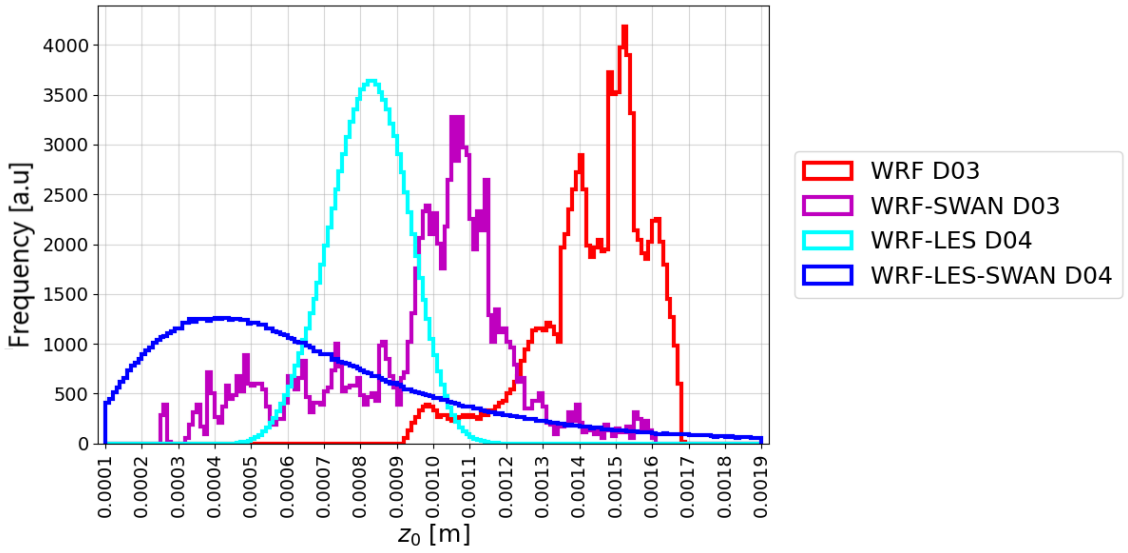


Figure 3. Distributions of simulated roughness length for D03 and D04 from coupled and uncoupled simulations for the 5th December, taken from several grid points around the RUNE locations.

3.2 Evaluation of simulated wave parameters

Figure 4 presents a comparison of H_s, MWD, and T_p derived from SWAN when coupled with both the mesoscale (D03) and LES (D04) domains against RUNE buoy measurements. The 10-min simulation outputs were averaged over hourly intervals

to match the temporal resolution of the hourly integrated measured wave parameters. The corresponding values of the root mean square error (RMSE) for each domain, calculated relative to the observations, are summarized in Table 2. The results indicate that, while model outputs in both domains follow the observed data, the LES-driven output provides improved wave characteristics, particularly for H_s, with an RMSE nearly half that of the mesoscale-driven domain output. The simulated T_p and MWD exhibit only minor differences between the two domains.

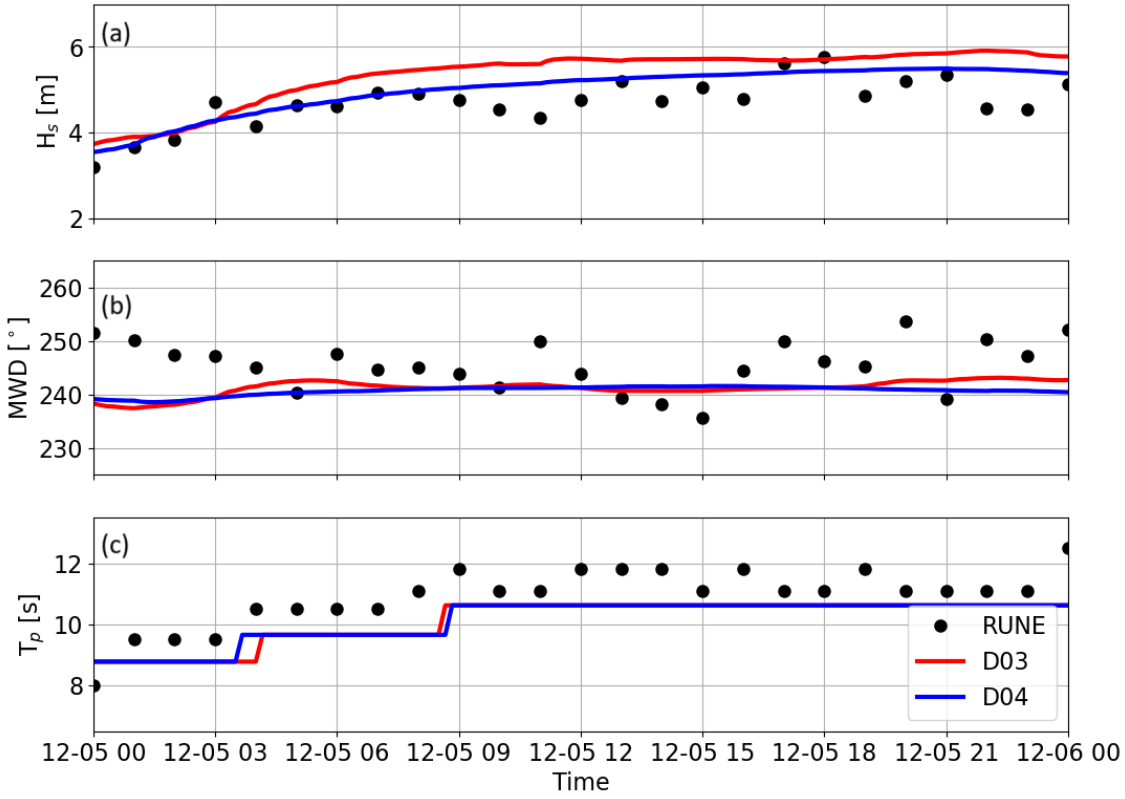


Figure 4. Hourly averaged time series of significant wave height (H_s) (a), mean wave direction (MWD) (b), and peak wave period (T_p) (c) from the coupled simulations of the mesoscale-driven (D03) and LES-driven (D04) domains, compared to wave buoy measurements on the 5th of December.

3.3 Evaluation of simulated mean flow

The time series of mean wind speed and direction output from both WRF-SWAN (coupled) and WRF (uncoupled) simulations of the mesoscale D03 domain and the LES D04 domain are compared against the lidar measurements at four different heights, 40, 79, 97, and 147 m, in Fig. 5. To ensure temporal consistency with the mesoscale results and measurements, the LES outputs were averaged over 10-min intervals from the 10-s output. At 40 m (a4), the lowest measurement height, simulations from the LES domain (both WRF-LES-SWAN and WRF-LES) show better agreement, in terms of magnitude and variability,

Table 2. The root mean square error (RMSE) computed between observations and simulations. The simulated significant wave height (H_s), mean wave direction (MWD), peak period (Tp), wind speed and wind direction are from the D03 and D04 model outputs. WRF and WRF-SWAN are taken from D03 for the uncoupled and coupled simulations, while WRF-LES and WRF-LES-SWAN are taken from D04. The wind speed and direction statistics are calculated for each of the heights from 40 up to 147 m and then averaged.

Variable	WRF-SWAN	WRF-LES-SWAN	WRF	WRF-LES
H_s [m]	0.75	**0.44**	–	–
MWD [°]	**6.61**	7.02	–	–
Tp [s]	0.97	**0.92**	–	–
Wind speed [m s^{-1}]	2.71	**1.81**	2.28	1.87
Wind direction [°]	**2.48**	3.06	**2.48**	3.16

with observations than those from the mesoscale domain. At 79 m(a3), the WRF-LES-SWAN run exhibits the best agreement with measurements. Above 97 m, WRF-LES-SWAN tends to overestimate the wind speed compared to observations, and above 147 m, the WRF-LES run also overestimates the observed wind speed, which can primarily be attributed to the effect of boundary conditions, as ERA5 overestimates the measurements by up to 3 m s^{-1} at some time steps. The higher simulated wind speeds in the coupled versus uncoupled simulations and the LES versus mesoscale simulations are consistent with the decreased simulated roughness length as shown in Figure 3.

Figure 6 presents the vertical profiles of wind speed and direction during the 2-hr period surrounding the time of maximum wave height (Hours 17:00 to 19:00 in Figure 2). Both WRF-LES and WRF-LES-SWAN runs provide wind speeds lower than observations near the surface; however, they result in an overall good agreement with measured mean wind speed between 40 and 150 m, as also evident in the RMSE values (Table 2) and timeseries (Figure 5). However, this is likely due to excessive vertical wind shear, which is attributed to the type of SGS model used for the LES domains (Peña and Mirocha, 2024; Sullivan et al., 1994; Gadde et al., 2021). In contrast, WRF and WRF-SWAN show wind profiles with vertical wind shears that are more consistent with those from the measurements, although both with a systematic bias at all measured levels. In addition, slightly higher wind speeds are observed in the coupled simulations compared to the uncoupled ones. The WBLM, which accounts for wave impacts and calculates an effective roughness length, can yield lower roughness length values than those from the Charnock-based parameterization (Charnock, 1955) used by default in the WRF model, particularly under storm conditions. Lower roughness lengths lead to higher surface wind speeds under the same forcing conditions; similar results were reported by Larsén et al. (2019) under stormy conditions. This is also reflected in our analysis of Figure 3. In terms of wind direction, both WRF-LES and WRF-LES-SWAN runs show a slight eastward deviation, with a maximum of approximately 4° up to 100 m, which results from lower simulated u velocities within the LES domains that are the product of the excessive vertical wind shear discussed earlier.

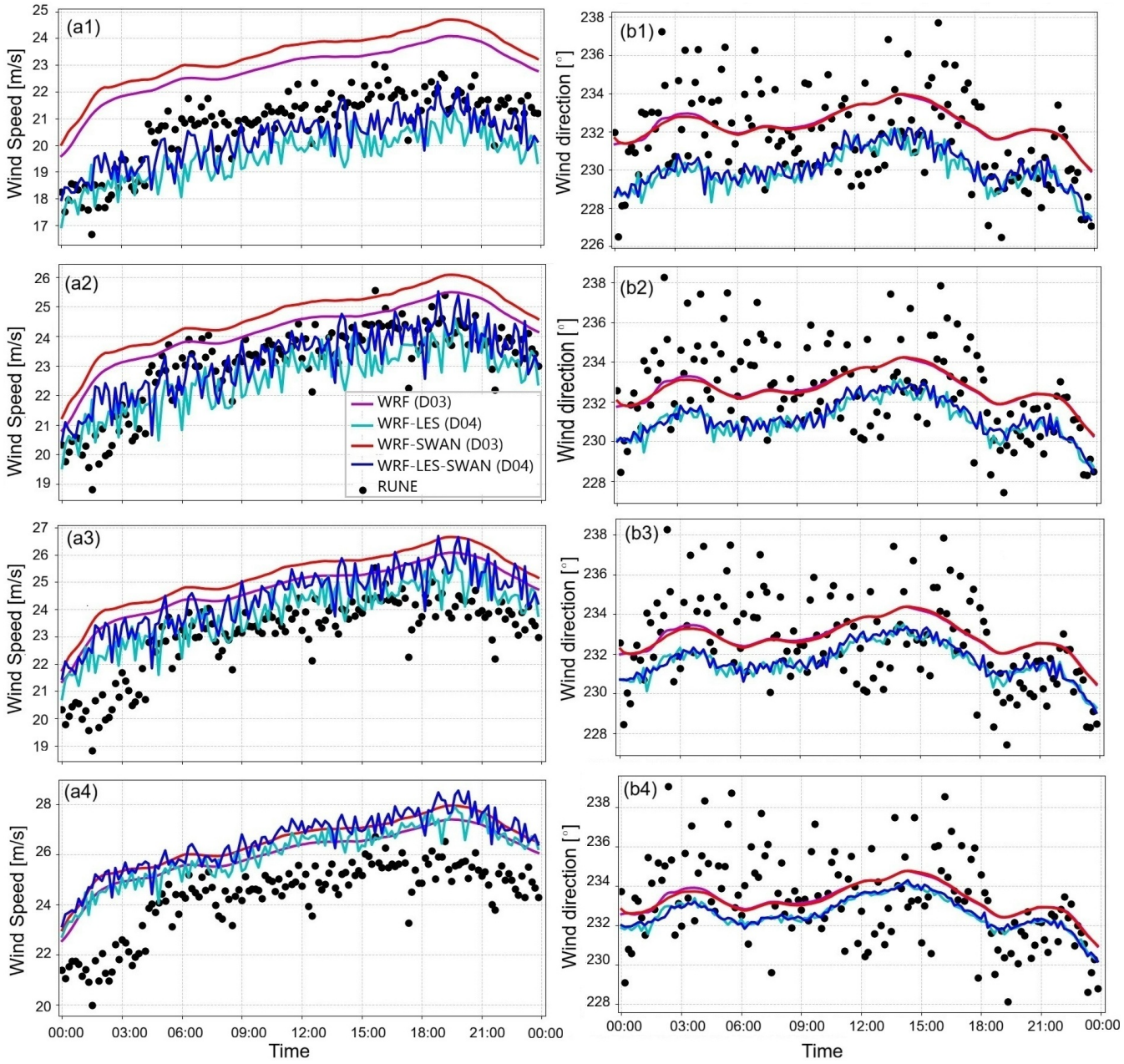


Figure 5. Time series of 10-min means of simulated (a*) wind speed and (b*) wind direction from the mesoscale (D03) and LES (D04) domains for both coupled (WRF-SWAN) and uncoupled (WRF) simulations, compared to lidar buoy data. Panels (a1–a4) correspond to wind speed at heights of 147 m, 97 m, 79 m, and 40 m, respectively. Panels (b1–b4) show wind direction at the same heights.

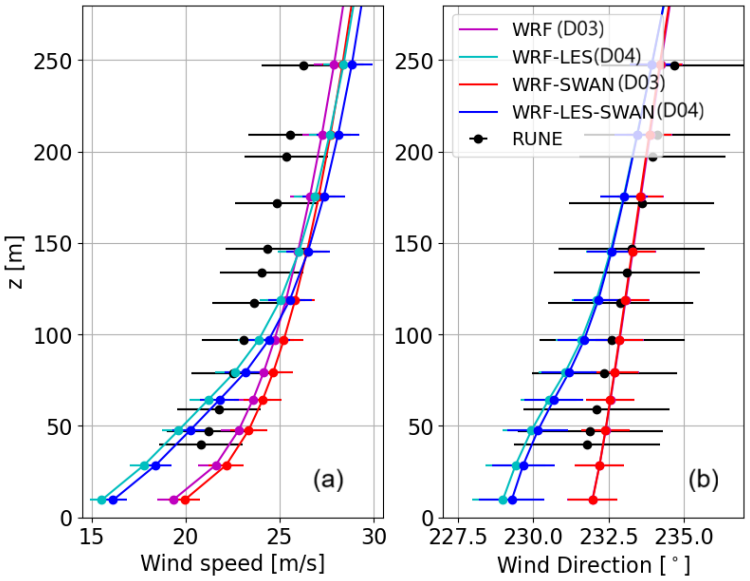


Figure 6. Vertical profiles of (a) wind speed and (b) wind direction over the period 17:00 UTC to 19:00 UTC from the D03 and D04 domains, for both coupled and uncoupled simulations, compared with lidar buoy measurements from 17:00 UTC to 19:00 UTC.

3.4 Turbulent fluxes

Although no high-frequency measurements are available for in-depth validation of the simulations, we investigate the behavior of turbulent fluxes of the coupled and uncoupled simulations using results from the LES domains. For this, we compute both the resolved and the SGS stress components. To capture the extreme event at the RUNE measurement location, we use 10-s model outputs over a 2-hr period from 02:00 UTC to 04:00 UTC. The resolved (res) stress components (τ_{ij}) for each velocity pair are computed as

$$\tau_{ij}^{\text{res}} = -\rho\langle u_i' u_j' \rangle, \tag{1}$$

where ρ is the air density, u_i and u_j are the along-wind and cross-wind components, the primes ($'$) denote fluctuations from the mean value, which are computed as a 10-min time average at the grid point closest to the measurement site, and the angle brackets $\langle\cdot\rangle$ indicate a temporal average.

The SGS part of the stress includes the deviatoric component τ_{ij}^{dev} and the part from the SGS turbulent kinetic energy e_{sgs}. Using the 10-s model outputs (D04 outputs e_{sgs} and the deviatoric stresses), the SGS stress is calculated as

$$\tau_{ij}^{\text{sgs}} = \frac{2}{3}\delta_{ij} e_{\text{sgs}} + \tau_{ij}^{\text{dev}}, \tag{2}$$

and the total stress components are obtained from

$$\tau_{ij}^{\text{tot}} = \tau_{ij}^{\text{res}} + \langle \tau_{ij}^{\text{sgs}} \rangle. \tag{3}$$

Figure 7 shows the vertical profiles of the velocity variances $\langle u'u' \rangle$, $\langle v'v' \rangle$, and $\langle w'w' \rangle$, as well as the covariances $\langle u'w' \rangle$ and $\langle v'w' \rangle$. The figure includes both resolved and total (resolved + SGS) fluxes from the WRF-LES and WRF-LES-SWAN runs at horizontal grid spacings of 100 m (D04) and 4 m (D06). The covariances $\langle u'w' \rangle$ and $\langle v'w' \rangle$ exhibit similar trends, with smaller resolved turbulence for D04 compared to D06, as expected from the effect of the spatial resolution difference. Results from both domains clearly show increased turbulence levels when wind–wave interactions are included in the simulation. Similar enhancements in velocity variances were also observed in an idealized simulation of the same case (Hamzeloo et al., 2025). For D04, the horizontal velocity variances have a maximum at around 70 m, which is rather far from the surface. This is an effect of the coarse horizontal grid spacing of D04 (100 m), a domain that cannot resolve the small eddies close to the surface. When finer horizontal grid spacings of 20 m (D05) and 4 m (D06) are used, the heights of the maximum turbulence fluxes appear closer to the surface, at a height of 60 m and 30 m, respectively. In Hamzeloo et al. (2025), a horizontal grid spacing of 1.25 m was used, and the corresponding height of the maximum turbulence fluxes was confined below the first 5 m. The contribution of SGS stresses is also more evident in D04 compared to D05 (not shown) and D06, as expected. The resolved vertical variances (dashed lines in Fig. 7c) are small in D04, and reach more realistic values (up to 0.1 $\mathrm{m^2\ s^{-2}}$) in D06.

As no turbulence measurements are available from the RUNE campaign, these differences in turbulence should be interpreted as physics-based model behavior rather than validated improvement. It is also important to mention that all domains share the same spin-up period, and despite the shorter total runtime of D05 and D06, the turbulence fields in these fine LES nests are well developed, as indicated by the larger resolved variances relative to D04. The shorter runtime primarily limits the length of the available time series rather than the development of turbulence. The D05 and D06 domains are therefore included to illustrate how increasing horizontal resolution modifies the balance between resolved and SGS turbulence.

3.5 The impact of cell perturbation method

Figure 8 shows the 24-hr time series of wind speed at 40 m from the nested LES domain (D04), with and without CPM. The results highlight the role of CPM in enhancing wind speed variability and fluctuations.

To further detail the enhancement of turbulence by using CPM, we compute in Fig. 9 the wind speed spectrum from lidar measurements, the finest mesoscale domain (D03), and the nested LES domain (D04), both with and without CPM. The spectrum is an average of spectra derived within 5-hr windows with a 15-min overlap. As illustrated, the spectrum from the no-CPM case fails to capture the levels of turbulent energy in the measurements even at time scales much larger than 10-min and closely resembles the mesoscale spectrum, which is not expected to resolve turbulence. In contrast, the D04 simulation with CPM activated matches more closely the spectral energy distribution of the measurements. The drop of energy at higher frequencies of the spectrum for WRF-LES with CPM can be noticed beyond the timescale of 1-min, which shows the limitation of coarse LES runs to properly reproduce a wide range of turbulence scales.

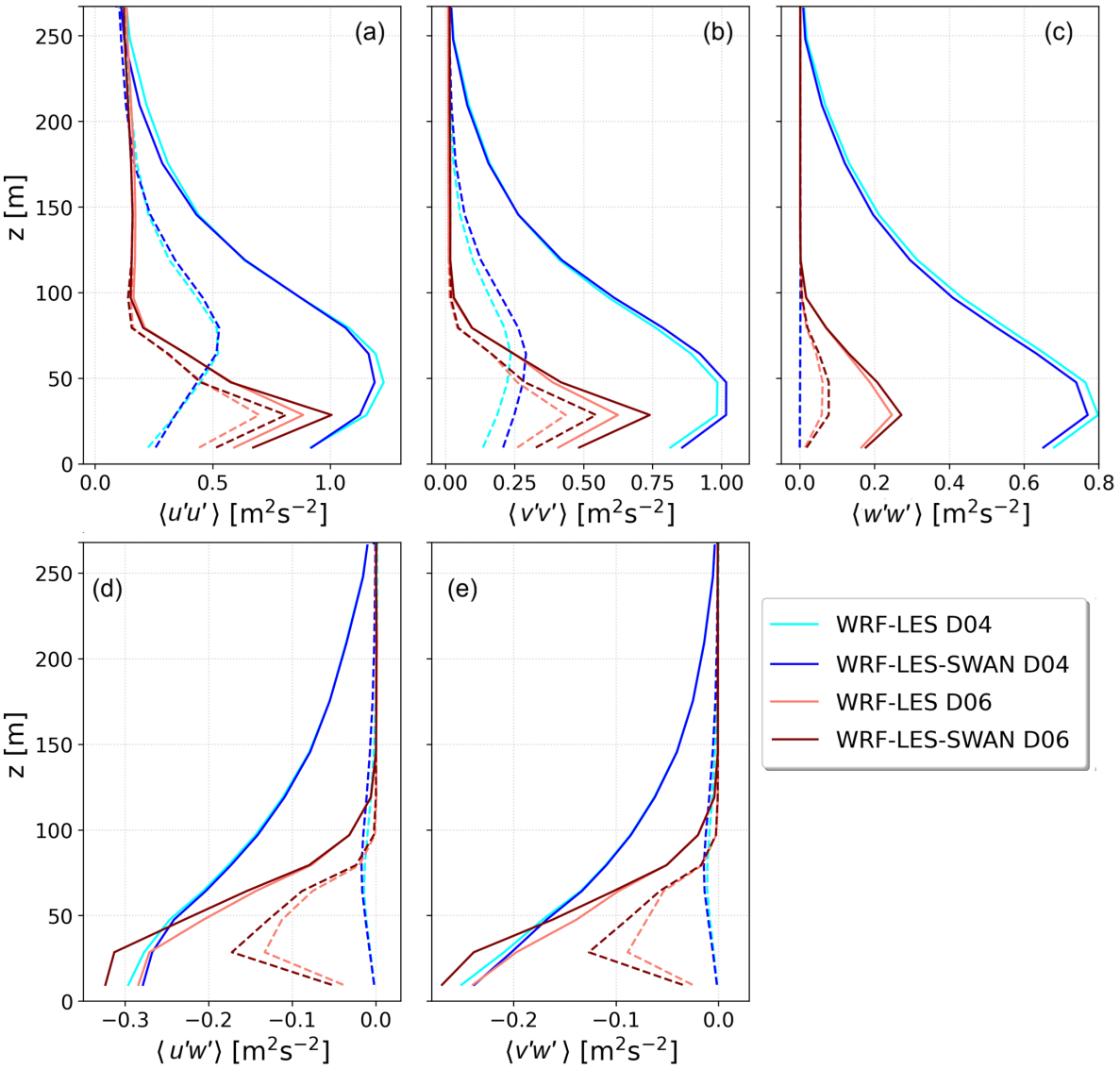


Figure 7. Vertical profiles of velocity variances (a) $\langle u'u' \rangle$, (b) $\langle v'v' \rangle$, (c) $\langle w'w' \rangle$, and covariances (d) $\langle u'w' \rangle$, (e) $\langle v'w' \rangle$ from WRF-LES and WRF-SWAN-LES runs at 100 m (D04) and 4 m (D06) horizontal grid spacings. Dashed and solid lines represent resolved and total (resolved + SGS) fluxes, respectively.

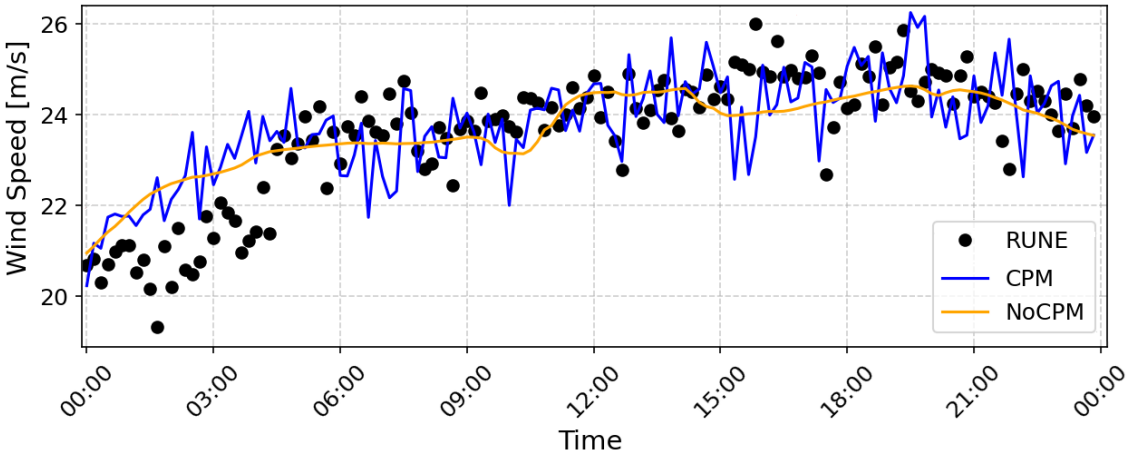


Figure 8. 10-min time series of wind speed at 100 m from the D04 simulation, with and without activating the CPM, compared to that from measurements.

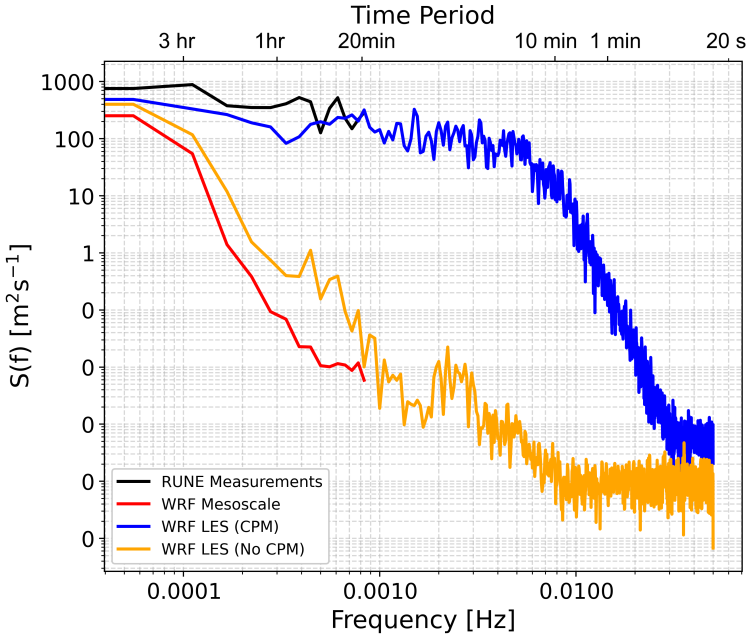


Figure 9. Spectrum of wind speed at 100 m from the mesoscale domain (D03), the LES domain (D04) both with and without CPM, and the RUNE measurements.

4 Discussion

We successfully coupled the WRF model in LES mode with the SWAN wave model within the COAWST system. This allows an examination of the air-sea interaction at high spatial and temporal resolution within the coupled model system. We tested this new system with a case study, which is a storm event in the North Sea, previously studied in Hamzeloo et al. (2025). Following the latter study, we chose this day due to the availability of measurements, both for the atmosphere and waves, and because it is a one-year return event, which is relevant for offshore wind and wave operational purposes. In addition, the wave age $c_p/U_{10} < 1.2$ (c_p is wave phase speed) during the simulated period suggests that waves are young and growing as also shown in Figure 2. Thus, it is a relatively easy case to start with testing our new coupled modeling system.

The comparison between coupled and uncoupled LES runs shows that wave–atmosphere interactions have a measurable impact on both mean flow and turbulence characteristics. The improved agreement in the significant wave height and mean wind speed up to 100 m when using the coupled WRF-LES-SWAN model indicates the importance of the online coupling, as their feedback modifies the exchanges in the WBL. This is mainly due to improvements in surface roughness and momentum fluxes estimations, which impact the wind field near the ocean surface. However, the relatively small differences in mean wave direction and peak wave period show that not all wave parameters are equally sensitive to the coupling, and the benefits may depend on the specific conditions of the event. The vertical wind profiles indicate that the better statistics on mean winds in Table 2 for the LES runs are achieved due to excessive vertical wind shear in LES near the surface, which is most probably caused by the SGS model. In contrast, the mesoscale simulations reproduce the vertical wind shear and veer close to that of the observations, although the LES runs capture greater variability in wind speed. All of the simulations have a bias in the upper atmospheric levels, which might be due to a bias in boundary conditions.

Note also that the 1-day storm case, although ideal for an initial test of the new coupled modeling system, does not represent the wide range of sea states that the North Sea experiences. Often, the North Sea sea state is complex with the presence of both wind-generated waves and swell, with waves aligned or misaligned with the wind. Measurements suggest that the air-sea momentum exchanged can be reduced or enhanced depending on the alignment of swell and wind sea (Larsén, 2003). The effect of non-local swell and its misalignment with the wind sea has been previously implemented in different wave models in e.g. Wu et al. (2016); Porchetta et al. (2019). Swell can also develop locally from the wind sea; with a varying wind field with changing wind direction, it can be mixed together with the waves generated locally, resulting in misalignment. The current modeling system using WBLM includes the swell developed locally and hence the associated misalignment (Fischereit et al., 2022). It is in our interest in the future to examine how our modeling system performs and potentially how to improve its performance in such complicated sea states.

The analysis shows that the coupled simulation produces higher horizontal and vertical velocity variances, which suggests enhanced turbulent mixing. This finding is consistent with theoretical expectations (Sullivan et al., 2008) and our previous modeling efforts (Hamzeloo et al., 2025). Due to the absence of direct turbulence measurements at the RUNE site, we are not able to quantify the accuracy of the turbulence simulations. At the beginning of our analysis, we examine the results from domain D04 with a horizontal grid spacing of 100 m. In this configuration, the vertical distribution of turbulence fluxes

shows the largest value at 70-m height and unrealistically small vertical velocity variances. For finer horizontal grid spacings, $\Delta x = 20$ m, the largest turbulence fluxes were present at slightly lower heights. With further refinement, Δx =4 m, the largest turbulence fluxes are at a height of around 25 m, and the vertical velocity variance reached more realistic magnitudes. The analysis confirms that fine horizontal grid spacing is essential for capturing the turbulence characteristics close to the surface and within a significant portion of the MABL. This is in agreement with the results in Sanchez-Gomez et al. (2025), who performed a multiscale simulation with two nested LES domains around Hurricane Laura, using horizontal grid spacings of 33.33 m and 11.11 m. They found that the coarsest simulation could not resolve turbulence close to the surface, while the finer resolution matched the turbulence statistics of the measurements.

Furthermore, two distinct processes contribute to the observed turbulence differences in our study shown in Figure 7. The increase from D03 to D04 arises from the change in turbulence representation when moving from a mesoscale PBL scheme to the LES SGS model, combined with the resolution dependence of the resolved–SGS partition at 100 m. In contrast, the differences between the coupled and uncoupled simulations within the same domain represent the physical impact of wind–wave coupling: the WBLM modifies the effective roughness and near-surface stress, enhancing shear production of turbulence. The finer LES domains (D05 and D06) further illustrate that increasing horizontal resolution increases the fraction of turbulence explicitly resolved.

The grid-spacing jump from D03 (1100 m) to D04 (100 m) is larger than typically recommended, but was necessary to reach LES-permitting resolution while keeping the multiscale simulation computationally feasible. This choice also avoids the gray zone (300–1000 m), where neither a PBL scheme nor LES is appropriate (Arthur et al., 2025; Juliano et al., 2022; **?**). With sufficient fetch and the use of the CPM, turbulence develops in D04 despite the large ratio. The vertical-to-horizontal grid-spacing ratio of about 10:1 in D04 is common in WRF mesoscale configurations and does not cause numerical instability; however, for LES it can influence how much near-surface turbulence is explicitly resolved and increases reliance on SGS stresses. This behavior is reflected in the turbulence profiles of D04 (Figure 7).

Note that in our simulation using the COAWST modeling system, we only activated the atmospheric and wave models. It would be of great interest in the future to couple the ocean model as well; it is expected that with more frequent and accurate updates of sea surface temperature through the ocean model, some storm characteristics will be improved (Li and Tan, 2023). It is also expected that during storm conditions, water currents in certain areas, e.g. shallow water regions, would also affect the air-sea interaction. Although this feedback may affect wave development and near-surface stability in shallow shelf regions, our previous analysis of this storm showed that the event behaved as a deep-water wave case based on the(Forristall, 2000) curve, suggesting that depth-related effects were limited during the selected period (Hamzeloo et al., 2025).

It is important to note, however, that SWAN is a phase-averaged wave model and does not resolve wave phases, even if the WRF-LES grid spacing is comparable to the wave wavelength. In the coupled system, waves affect the atmosphere only through phase-averaged quantities such as roughness length and surface stress. Therefore, the LES represents flow over a sea-state-dependent rough surface, not over phase-resolved moving waves. Wave-coherent effects are also not captured, which is a limitation of this approach.

In addition, we evaluate the impact of the CPM on the LES domain boundaries, which is applied for the first time in the WRF model through the COAWST framework. In the simulation without CPM, the LES domain cannot sustain turbulence, and the results are similar to those of the mesoscale domain. More importantly, the ensemble-averaged wind speed spectrum indicates that the LES without CPM fails capturing the expected turbulence energy levels, even at the time scales larger than those of 3D turbulence. In contrast, LES with CPM produces more realistic spectral energy distributions within a wider range of scales, consistent with previous real-time simulation studies (Peña and Mirocha, 2024).

5 Conclusions

In this study, we coupled the WRF-LES model with the SWAN model within the framework of COAWST. We applied the coupled, multiscale, modeling system to a real storm case, and evaluated the model performance in capturing mean wind and turbulence characteristics within the MABL.

Both coupled and uncoupled LES results showed better agreement with measurements at the heights closer to the surface due to excessive vertical wind shear reproduced within the LES domain. Compared to the standalone WRF or WRF-LES simulations, coupling does not show significant differences in the mean wind speed for this storm case, while it enhances the turbulence fluxes due to wave-modified surface roughness and pressure, although such enhancement could not be evaluated due to the absence of turbulence measurements. Turbulence in the layers close to the surface has been shown to be very sensitive to horizontal grid spacing. This study also shows that turbulence instigation (through CPM) is essential for reproducing realistic turbulence in LES domains over sea roughnesses.

For future work, we plan to perform multiscale simulations at a site where high-frequency turbulence measurements are available for in-depth analysis of turbulence characteristics. This will allow direct validation of simulated turbulence fluxes and help quantify the strengths and limitations of coupled WRF-LES-SWAN configurations under different wind–wave conditions. In addition, future studies should also investigate periods with different sea states, such as wind–wave misalignment and swell conditions, and the impact of modelled ocean dynamics through ROMS in the COAWST framework.

Appendix A: Abbreviations

CCI Climate Change Initiative

COAWST Coupled Ocean Atmosphere Wave Sediment Transport

CORINE Coordination of Information on the Environment

CPM Cell Perturbation Method

DHI Danish Hydraulic Institute

DTM Digital Terrain Model

DTU Technical University of Denmark

ECMWF European Centre for Medium-Range Weather Forecasts

EMODnet European Marine Observation and Data Network

ERA5 ECMWF Fifth-Generation Atmospheric Reanalysis

ESA European Space Agency

H_{max} Maximum wave height

H_s Significant wave height

JONSWAP Joint North Sea Wave Project

LES Large-Eddy Simulation

LiDAR Light Detection and Ranging

MABL Marine Atmospheric Boundary Layer

MIKE 3 Wave FM MIKE 3 Wave Flexible Mesh

MWD Mean Wave Direction

MYJ Mellor–Yamada–Janjic

MYNN Mellor–Yamada–Nakanishi–Niino

OSTIA Operational Sea Surface Temperature and Sea Ice Analysis

PALM Parallelized Large-Eddy Simulation Model

PBL Planetary Boundary Layer

QNSE Quasi-Normal Scale Elimination

RMSE Root Mean Square Error

ROMS Regional Ocean Modeling System

RRTM Rapid Radiative Transfer Model

RUNE Reducing the Uncertainty of Nearshore Energy

SGS Subgrid-Scale

SWAN Simulating WAves Nearshore

T_{02} Average zero-crossing period

TKE Turbulent Kinetic Energy

T_p Peak wave period

UTC Coordinated Universal Time

WAM Wave Model

WBL Wave Boundary Layer

WBLM Wave Boundary Layer Model

WRF Weather Research and Forecasting

WSM6 WRF Single-Moment 6-class microphysics scheme

YSU Yonsei University

Author contributions. SH implemented the changes in WRF and carried out the simulations and analysis. JF contributed to the understanding of the COAWST workflow, and OGS provided inputs on WRF-LES simulations. XGL, AP, and JF provided supervision and guidance throughout the work. SH wrote the initial manuscript draft. All authors reviewed and commented on the manuscript.

Competing interests. AP is a member of the editorial board of Wind Energy Science.

Acknowledgements. This work is funded by the Independent Research Fund Denmark (Danmarks Frie Forskningsfond DFF) through the 'multiscale Atmospheric Modeling Above the Seas (MAMAS)' project (nr. 0217-00055B). SH, XGL and JF acknowledge support from the Horizon Europe project DTWO (J. nr. 101146689). The authors also thank Marc Imberger and Jianting Du for their assistance regarding the COAWST system.

References

Alimohammadi, M., Malakooti, H., and Rahbani, M.: Comparison of momentum roughness lengths of the WRF-SWAN online coupling and WRF model in simulation of tropical cyclone Gonu, Ocean Dynamics, 70, 1531–1545, https://doi.org/10.1007/s10236-020-01417-w, 2020.

Arthur, R. S., Rybchuk, A., Juliano, T. W., Rios, G., Wharton, S., Lundquist, J. K., and Fast, J. D.: Evaluating mesoscale model predictions of diurnal speedup events in the Altamont Pass Wind Resource Area of California, Wind Energy Science, 10, 1187–1209, https://doi.org/10.5194/wes-10-1187-2025, 2025.

Bolaños, R. and Rørbæk, K.: RUNE, Metocean buoy deployment, Tech. rep., DHI, 2016.

Bontemps, S., Defourny, P., Radoux, J., Van Bogaert, E., Lamarche, C., Achard, F., Mayaux, P., Boettcher, M., Brockmann, C., Kirches, G., et al.: Consistent global land cover maps for climate modelling communities: current achievements of the ESA's land cover CCI, in: Proceedings of the ESA living planet symposium, Edimburgh, vol. 13, pp. 9–13, 2013.

Booij, N., Holthuijsen, L., and Ris, R.: The SWAN Wave Model for Shallow Water, pp. 668–676, American Society of Civil Engineers, https://doi.org/10.1061/9780784402429.053, 1997.

C3S: ERA5: Fifth generation of ECMWF atmospheric reanalyses of the global climate, https://cds.climate.copernicus.eu/cdsapp#!/home, accessed: [date of access], 2017.

Cambazoglu, M. K., Armstrong, B. N., and Wiggert, J. D.: Development of a daily coastal ocean model for Mississippi Sound and Bight, Ocean Dynamics, 74, 987–1004, https://doi.org/10.1007/s10236-024-01645-4, 2024.

Charnock, H.: Wind stress on a water surface, Quarterly Journal of the Royal Meteorological Society, 81, 639–640, https://doi.org/10.1002/qj.49708135027, 1955.

Chen, W., Chen, J., Shi, J., Zhang, S., Zhang, W., Xia, J., Wang, H., Yi, Z., Wu, Z., and Zhang, Z.: Impact of a New Wave Mixing Scheme on Ocean Dynamics in Typhoon Conditions: A Case Study of Typhoon In-Fa (2021), Remote Sensing, 16, https://doi.org/10.3390/rs16173298, 2024.

Chow, F. K., Schär, C., Ban, N., Lundquist, K. A., Schlemmer, L., and Shi, X.: Crossing Multiple Gray Zones in the Transition from Mesoscale to Microscale Simulation over Complex Terrain, Atmosphere, 10, https://doi.org/10.3390/atmos10050274, 2019.

Deardorff, J. W.: Stratocumulus-capped mixed layers derived from a three-dimensional model, Boundary-Layer Meteorology, 18, 495–527, https://doi.org/10.1007/BF00119502, 1980.

DHI: MIKE 3 Wave FM: Scientific Documentation, DHI Group, https://manuals.mikepoweredbydhi.help/2019/Coast_and_Sea/MIKE_3_Wave_FM_Scientific_Doc.pdf, 2024.

Donlon, C. J., Martin, M., Stark, J., Roberts-Jones, J., Fiedler, E., and Wimmer, W.: The Operational Sea Surface Temperature and Sea Ice Analysis (OSTIA) system, Remote Sensing of Environment, 116, 140–158, https://doi.org/10.1016/j.rse.2010.10.017, advanced Along Track Scanning Radiometer(AATSR) Special Issue, 2012.

Du, J.: Coupling atmospheric and ocean wave models for storm simulation, Ph.D. thesis, Technical University of Denmark, DTU Wind Energy, https://doi.org/10.11581/DTU:00000020, 2017.

Du, J., Bolaños, R., Larsén, X., and Kelly, M.: Wave boundary layer model in SWAN revisited, Ocean Science, 15, 361–377, https://doi.org/10.5194/os-15-361-2019, 2019.

Du, J., Larsén, X. G., Chen, S., Bolaños, R., Badger, M., and Yang, Y.: The impact of wind–wave coupling with WBLM on coastal storm simulations, Ocean Modelling, 180, 102 135, https://doi.org/10.1016/j.ocemod.2022.102135, 2022.

Dudhia, J.: Numerical Study of Convection Observed during the Winter Monsoon Experiment Using a Mesoscale Two-Dimensional Model, Journal of Atmospheric Sciences, 46, 3077 – 3107, https://doi.org/10.1175/1520-0469(1989)046<3077:NSOCOD>2.0.CO;2, 1989.

Feranec, J.: Project CORINE land cover, in: European Landscape Dynamics, pp. 39–44, CRC Press, 2016.

Fischereit, J., Larsén, X., and Hahmann, A.: Climatic Impacts of Wind-Wave-Wake Interactions in Offshore Wind Farms, Frontiers in Energy Research, 10, https://doi.org/10.3389/fenrg.2022.881459, 2022.

Floors, R., Peña, A., Lea, G., Vasiljević, N., Simon, E., and Courtney, M.: The RUNE Experiment—A Database of Remote-Sensing Observations of Near-Shore Winds, Remote Sensing, 8, 884, https://doi.org/10.3390/rs8110884, 2016.

Forristall, G. Z.: Wave Crest Distributions: Observations and Second-Order Theory, Journal of Physical Oceanography, 30, 1931 – 1943, https://journals.ametsoc.org/view/journals/phoc/30/8/1520-0485_2000_030_1931_wcdoas_2.0.co_2.xml, 2000.

Gadde, S. N., Stieren, A., and Stevens, R. J. A. M.: Large-Eddy Simulations of Stratified Atmospheric Boundary Layers: Comparison of Different Subgrid Models, Boundary-Layer Meteorology, 178, 363–382, https://doi.org/10.1007/s10546-020-00570-5, 2021.

Hamzeloo, S., Larsén, X., Peña, A., Kistne, S., and Soerensen, J.: Development of one-way coupling between MIKE 3 wave FM model and WRF-LES for the evaluation of a storm simulation, Boundary-Layer Meteorology, 191, https://doi.org/10.1007/s10546-025-00942-9, 2025.

Hong, S.-Y., Dudhia, J., and Chen, S.-H.: A Revised Approach to Ice Microphysical Processes for the Bulk Parameterization of Clouds and Precipitation, Monthly Weather Review, 132, 103 – 120, https://doi.org/10.1175/1520-0493(2004)132<0103:ARATIM>2.0.CO;2, 2004.

Hong, S.-Y., Noh, Y., and Dudhia, J.: A New Vertical Diffusion Package with an Explicit Treatment of Entrainment Processes, Monthly Weather Review, 134, 2318 – 2341, https://doi.org/10.1175/MWR3199.1, 2006.

Janjic, Z. I.: The Mellor–Yamada Level 2.5 turbulence closure scheme in the NCEP Eta Model, Office Note, National Centers for Environmental Prediction, 437, 2002.

Jiang, Z., Tang, J., Wang, S., Dong, G., and Wang, S.: Simulation of summer climate over East China by convection-permitting regional air-sea coupled model, Climate Dynamics, 63, 106, https://doi.org/10.1007/s00382-025-07589-9, 2025.

Juliano, T. W., Kosović, B., Jiménez, P. A., Eghdami, M., Haupt, S. E., and Martilli, A.: "Gray Zone" Simulations Using a Three-Dimensional Planetary Boundary Layer Parameterization in the Weather Research and Forecasting Model, Monthly Weather Review, 150, 1585–1619, https://doi.org/10.1175/MWR-D-21-0164.1, 2022.

Kain, J. S. and Fritsch, J. M.: Convective Parameterization for Mesoscale Models: The Kain-Fritsch Scheme, pp. 165–170, American Meteorological Society, Boston, MA, ISBN 978-1-935704-13-3, https://doi.org/10.1007/978-1-935704-13-3_16, 1993.

Kalvig, S., Reuder, J., and Byrkjedal, Ø.: Wave influenced wind and the effect on offshore wind turbine performance, in: European Wind Energy Association Conference, https://www.researchgate.net/publication/270282509_Wave_Influenced_Wind_and_the_Effect_on_Offshore_Wind_Turbine_Performance, 2014.

Kshetri, P. and Momen, M.: The Impacts of Sub-grid Scale Parameterization of Large-Eddy Simulations on Real Hurricane Dynamics and Forecasts, Boundary-Layer Meteorology, 191, 46, https://doi.org/10.1007/s10546-025-00939-4, 2025.

Larsén, X. G.: Air–Sea Exchange of Momentum and Sensible Heat Over the Baltic Sea, Ph.D. thesis, Uppsala University, https://backend.orbit.dtu.dk/ws/portalfiles/portal/8167484/Air_Sea_Exchange_of_Momentum.pdf, 2003.

Larsén, X., Fischereit, J., Hamzeloo, S., Bärfuss, K., and Lampert, A.: Investigation of wind farm impacts on surface waves using coupled numerical simulations, Renewable Energy, 237, https://doi.org/10.1016/j.renene.2024.121671, 2024.

Larsén, X. G., Du, J., Bolaños, R., Imberger, M., Kelly, M. C., Badger, M., and Larsen, S.: Estimation of offshore extreme wind from wind-wave coupled modeling, Wind Energy, 22, 1043–1057, https://doi.org/10.1002/we.2339, 2019.

Li, D.-Y. and Tan, Z.-M.: The Role of Ocean–Atmosphere Interactions in Tropical Cyclone Intensity Predictability, Journal of the Atmospheric Sciences, 80, 1213 – 1226, https://doi.org/10.1175/JAS-D-22-0152.1, 2023.

Mlawer, E. J., Taubman, S. J., Brown, P. D., Iacono, M. J., and Clough, S. A.: Radiative transfer for inhomogeneous atmospheres: RRTM, a validated correlated-k model for the longwave, Journal of Geophysical Research: Atmospheres, 102, 16 663–16 682, https://doi.org/10.1029/97JD00237, 1997.

Muñoz-Esparza, D. and Kosović, B.: Generation of inflow turbulence in large-eddy simulations of nonneutral atmospheric boundary layers with the cell perturbation method, Monthly Weather Review, 146, 1889–1909, https://doi.org/10.1175/MWR-D-18-0077.1, 2018.

Muñoz-Esparza, D., Kosović, B., Mirocha, J., and van Beeck, J.: Bridging the Transition from Mesoscale to Microscale Turbulence in Numerical Weather Prediction Models, Boundary-Layer Meteorology, 153, 409–440, https://doi.org/10.1007/s10546-014-9956-9, 2014.

Muñoz-Esparza, D., Kosović, B., van Beeck, J., and Mirocha, J.: A stochastic perturbation method to generate inflow turbulence in large-eddy simulation models: Application to neutrally stratified atmospheric boundary layers, Physics of Fluids, 27, 035 102, https://doi.org/10.1063/1.4913572, 2015.

Muñoz-Esparza, D., Lundquist, J. K., Sauer, J. A., Kosović, B., and Linn, R. R.: Coupled mesoscale-LES modeling of a diurnal cycle during the CWEX-13 field campaign: From weather to boundary-layer eddies, Journal of Advances in Modeling Earth Systems, 9, 1572–1594, https://doi.org/https://doi.org/10.1002/2017MS000960, 2017.

Nakanishi, M. and Niino, H.: An improved Mellor–Yamada level-3 model: Its numerical stability and application to a regional prediction of advection fog, Boundary-Layer Meteorology, 119, 397–407, https://doi.org/10.1007/s10546-005-9030-8, 2006.

Ning, X., Paskyabi, M. B., Bui, H. H., and Penchah, M. M.: Evaluation of sea surface roughness parameterization in meso-to-micro scale simulation of the offshore wind field, Journal of Wind Engineering and Industrial Aerodynamics, 242, 105 592, https://doi.org/10.1016/j.jweia.2023.105592, 2023.

Olabarrieta, M., Warner, J., Armstrong, B., Zambon, J., and He, R.: Ocean-atmosphere dynamics during Hurricane Ida and Nor'Ida: An application of the coupled ocean-atmosphere-wave-sediment transport (COAWST) modeling system, Ocean Modelling, 43-44, 112–137, https://doi.org/https://doi.org/10.1016/j.ocemod.2011.12.008, 2012.

Peña, A. and Mirocha, J. D.: One-year-long turbulence measurements and modeling using large-eddy simulation domains in the Weather Research and Forecasting model, Applied Energy, 363, 123 069, https://doi.org/10.1016/j.apenergy.2024.123069, 2024.

Porchetta, S., Temel, O., Muñoz-Esparza, D., Reuder, J., Monbaliu, J., van Beeck, J., and van Lipzig, N.: A new roughness length parameterization accounting for wind–wave (mis)alignment, Atmospheric Chemistry and Physics, 19, 6681–6700, https://doi.org/10.5194/acp-19-6681-2019, 2019.

Sanchez-Gomez, M., Deskos, G., and Lundquist, J. K.: Turbulence-resolving simulations of Hurricane Laura (2020): Insights into extreme winds and eyewall turbulence, Quarterly Journal of the Royal Meteorological Society, https://doi.org/10.1002/qj.70003, first published: 29 August 2025, 2025.

Shaw, W. J., Berg, L. K., Debnath, M., Deskos, G., Draxl, C., Ghate, V. P., Hasager, C. B., Kotamarthi, R., Mirocha, J. D., Muradyan, P., Pringle, W. J., Turner, D. D., and Wilczak, J. M.: Scientific challenges to characterizing the wind resource in the marine atmospheric boundary layer, Wind Energy Science, 7, 2307–2334, https://doi.org/10.5194/wes-7-2307-2022, 2022.

Skamarock, W., Klemp, J., Dudhia, J., Gill, D., Liu, Z., Berner, J., and Huang, X.-y.: A description of the advanced research WRF model version 4.1, 2019.

Sukoriansky, S., Galperin, B., and Perov, V.: A quasi-normal scale elimination model of turbulent flows with stable stratification, Physics of Fluids, 17, 085 107, https://doi.org/10.1063/1.2009010, 2005.

Sullivan, P. P., McWilliams, J. C., and Moeng, C.-H.: A subgrid-scale model for large-eddy simulation of planetary boundary-layer flows, Boundary-Layer Meteorology, 71, 247–276, https://doi.org/10.1007/BF00713741, 1994.

Sullivan, P. P., Edson, J. B., Hristov, T., and McWilliams, J. C.: Large-Eddy Simulations and Observations of Atmospheric Marine Boundary Layers above Nonequilibrium Surface Waves, Journal of the Atmospheric Sciences, 65, 1225 – 1245, https://doi.org/10.1175/2007JAS2427.1, 2008.

Tewari, M., Chen, F., Wang, W., Dudhia, J., LeMone, M. A., Mitchell, K., Ek, M., Gayno, G., Wegiel, J., and Cuenca, R. H.: Implementation and verification of the unified Noah land surface model in the WRF model, in: 20th Conference on Weather Analysis and Forecasting/16th Conference on Numerical Weather Prediction, American Meteorological Society, https://opensky.ucar.edu/islandora/object/conference%3A1576, 2004.

Vortex FdC: Validation of Vortex-LES for Europe, https://www.vortexfdc.com/assets/docs/validation_LES_EUROPE.pdf, accessed: 2026-01-06, 2018.

Warner, J., Armstrong, B., He, R., and Zambon, J.: Development of a Coupled Ocean–Atmosphere–Wave–Sediment Transport Modeling System, Ocean Modelling, 35, 230–244, https://doi.org/https://doi.org/10.1016/j.ocemod.2010.07.010, 2010.

Wu, L., Rutgersson, A., Sahlée, E., and Larsén, X. G.: Swell impact on wind stress and atmospheric mixing in a regional coupled atmosphere–wave model, Journal of Geophysical Research: Oceans, 121, 4633–4648, https://doi.org/10.1002/2015JC011576, 2016.

Yang, X., Shen, L., and Sotiropoulos, F.: Large-eddy simulations of wind–wave–turbine interactions over the ocean, Journal of Fluid Mechanics, 755, R1, https://doi.org/10.1017/jfm.2014.396, 2014.